



**HAL**  
open science

## Post-process lasering improves strength-ductility tradeoff and fatigue limit of additively manufactured stainless steels

Juan Guillermo Santos Macías, Kewei Chen, Alexandre Tanguy, Maxime Vallet, Louis Cornet, Vincent Michel, Manas Vijay Upadhyay

### ► To cite this version:

Juan Guillermo Santos Macías, Kewei Chen, Alexandre Tanguy, Maxime Vallet, Louis Cornet, et al.. Post-process lasering improves strength-ductility tradeoff and fatigue limit of additively manufactured stainless steels. 2024. hal-04530203v2

**HAL Id: hal-04530203**

**<https://hal.science/hal-04530203v2>**

Preprint submitted on 6 Oct 2024

**HAL** is a multi-disciplinary open access archive for the deposit and dissemination of scientific research documents, whether they are published or not. The documents may come from teaching and research institutions in France or abroad, or from public or private research centers.

L'archive ouverte pluridisciplinaire **HAL**, est destinée au dépôt et à la diffusion de documents scientifiques de niveau recherche, publiés ou non, émanant des établissements d'enseignement et de recherche français ou étrangers, des laboratoires publics ou privés.



Distributed under a Creative Commons Attribution 4.0 International License

# Post-process lasering improves strength-ductility tradeoff and fatigue limit of additively manufactured stainless steels

Juan Guillermo Santos Macías<sup>1,a,\*</sup>, Kewei Chen<sup>1</sup>, Alexandre Tanguy<sup>1</sup>, Nathalie Isac<sup>1</sup>, Maxime Vallet<sup>2,3</sup>, Louis Cornet<sup>2</sup>, Vincent Michel<sup>4</sup>, Manas Vijay Upadhyay<sup>1,\*</sup>

<sup>1</sup> Laboratoire de Mécanique des Solides (LMS), CNRS, École Polytechnique, Institut Polytechnique de Paris, Route de Saclay, 91120 Palaiseau, France

<sup>2</sup> Université Paris-Saclay, CentraleSupélec, ENS Paris-Saclay, CNRS, LMPS - Laboratoire de Mécanique Paris-Saclay, 91190 Gif-sur-Yvette, France

<sup>3</sup> Université Paris-Saclay, CentraleSupélec, CNRS, Laboratoire SPMS - Structures, Propriétés et Modélisation des Solides, 91190 Gif-sur-Yvette, France

<sup>4</sup> Laboratoire de Procédés et Ingénierie en Mécanique et Matériaux (PIMM), CNRS UMR 8006, Arts et Metiers Institute of Technology, HESAM University, 151 Boulevard de l'Hôpital, 75013 Paris, France

\* Corresponding author email:

[manas.upadhyay@polytechnique.edu](mailto:manas.upadhyay@polytechnique.edu)  
[guillermo.santos@imdea.org](mailto:guillermo.santos@imdea.org)

## Abstract

Although stainless steels fabricated via additive manufacturing exhibit higher strength in comparison to their conventionally manufactured counterparts, they often suffer from lower ductility and poorer fatigue limit. In this work, post-process micron-sized lasering is used to re-engineer additively manufactured stainless steel microstructures close to the sample surface in order to improve their overall performance. The key idea is to use smaller spot sizes and faster scan speeds during post-process lasering compared to the fabrication process. Using a novel coupling between a continuous-wave laser and a scanning electron microscope, single line scans were performed to optimise the lasering parameters. The optimised parameters were then used to treat the surface of the entire sample. The result is an intragranular structure refinement near the surface, exhibiting nearly an order of magnitude reduction in microsegregation cell and dislocation structure size, and increase in dislocation density. The ensuing microstructure demonstrates a higher yield strength without ductility loss and significant enhancement of the fatigue limit due to reduced surface roughness and intragranular structure refinement. The proposed technique has tremendous potential to improve the mechanical response of alloys fabricated either via additive manufacturing or any other manufacturing technique.

## Keywords

Laser treatment, mechanical behaviour, electron microscopy, fatigue, 3D printing

<sup>a</sup> Current address: Instituto madrileño de estudios avanzados materiales (IMDEA materiales), Calle Eric Kandel 2, 28906 Getafe, Spain

## 1. Introduction

One of the most important goals of research on engineering of stainless steels is to design microstructures that exhibit higher strength, ductility and fatigue limit than currently possible while reducing energy and material consumption. The advent of metal additive manufacturing (AM), has opened up the possibility to design as built (AB) parts with microstructures that present unprecedentedly higher strengths in comparison to their conventionally manufactured counterparts [1]. However, this increase in strength is often accompanied by a decrease in ductility and a poorer fatigue response [2], which is affected by a combination of material strength, surface roughness, defects (porosities or voids) and the residual stress state.

At the origin of the strength-ductility trade-off lies the hierarchical microstructure arising from the highly non-equilibrium processes occurring during AM. Heat-matter interaction induced melt pool dynamics, rapid solidification and solid-state thermal cycling result in a microstructure exhibiting physical and chemical heterogeneities ranging from few tens of nanometres to several hundreds of micrometres [3,4]. The primary contribution to material strength arises from the smallest of these features, which in stainless steels are precipitates, microsegregation cells, dislocation structures including low angle grain boundaries [5]. These intragranular features determine the mean free path of plastic deformation accommodating defects such as mobile dislocations. Typically, the smaller the size and higher the density of these features, the higher the strength and lower the ductility [1]. A commonly used approach to improve ductility is annealing, which is an isothermal heat treatment that evolves the metastable AB microstructure towards equilibrium by minimizing the stored energy. However, this process inadvertently causes an increase in feature size and decrease in density, inevitably resulting in a decrease in strength.

Meanwhile, the fatigue response of dense (negligible amount of porosities/voids) AB parts rely on the material strength as well as surface roughness [6]. During AM, unmelted powder particles sinter to the surface and become the dominant contributors to surface roughness of AB parts. Under fatigue loading, failure mainly occurs from surface crack nucleation (if not already present) and propagation in dense alloys. The fatigue response of AB parts can be improved via post-process surface treatments, the most common of which are mechanical in nature e.g., shot peening, polishing, etc., that induce in-plane compressive stresses on the surface and reduce surface roughness.

In this investigation, a non-isothermal heat treatment for AB parts is proposed in the form of continuous-wave (CW) laser scanning that simultaneously alters the underlying microstructure, specifically significantly refines the intragranular structure, and improves surface quality. The key idea is to perform this laser scanning using spot sizes and scanning speeds that are respectively smaller and faster than those used to build the samples in order to simultaneously improve the surface roughness and alter the intragranular microstructure. Parameters that lead to surface remelting and fast cooling rates are used to refine the microstructure and produce a significant enhancement in mechanical properties.

This idea has been motivated by the microstructural differences between AB stainless steels fabricated via two commonly used techniques: CW laser-based powder bed fusion (LPBF) and CW laser-based direct energy deposition (LDED). LPBF processes use smaller laser spot sizes and faster scanning speeds than LDED processes. Consequently, stainless steel microstructures fabricated via LPBF exhibit smaller and denser features, and hence higher strength and lower

ductility, than the LDED ones [4]. In this work, LDED stainless steel samples were used as base material and their surfaces were laser scanned using spot sizes and scan speeds corresponding to LPBF. Note that while post-process laser-based surface treatments have been applied to polish surfaces of AM alloys [7,8] i.e., to reduce their surface roughness, they have not been used to simultaneously refine the intragranular structure and improve surface roughness, both of which are important to improve the overall mechanical response of a material.

In this work, the treatment is performed on two different alloys, 316L and 316LSi, to explore its reproducibility and versatility. The compositions of these two materials differ mainly in their Si content. The addition of Si increases the Cr equivalent to Ni equivalent ratio and, together with the cooling rates experienced during LDED, results in icosahedral short-range order-based grain nucleation in the melt and ferrite to massive austenite transformation mode in the solid state [9]. The resulting microstructure exhibits a very high proportion of low coincident site lattice boundaries and a higher proportion of the ferrite phase [9] causing an improvement in corrosion properties and mechanical behaviour (improvement in both strength and ductility) [10]. In general, 316L is interesting for its status as reference steel alloy in AM. 316LSi is particularly adequate in this research for its superior properties, which, if improved by the studied treatment, would further showcase its value. Indeed, the potential industrial application of this technique should include any AM alloy used where high strength, fatigue and corrosion resistance are needed (e.g. structural parts, transport industry, corrosive environments). Previous literature [7,8] has focused on the relevant corrosion aspect, hence this study covers the microstructure and surface state, closely linked to corrosion behaviour, but focuses on the effect on mechanical properties, also a paramount item in the field.

The following two main hypotheses are derived and developed upon in this research: The lasered material has smaller and denser dislocation structures and, thus, higher strength; lasered samples have longer fatigue life due to surface roughness reduction and strength increase.

The article is divided as follows: the experimental procedure and methods, including the CW laser-SEM, are described in section 2. Section 3 presents results and discussion around the parametric study, and tensile and fatigue testing. Finally, the conclusions of the study are presented.

## 2. Material and methods

### 2.1 Material

The materials studied in this work are two 316L stainless steels with different Si content. Henceforth, they are called 316L and 316LSi. Wrought alloys are used to manufacture 316L and 316LSi powders via inert gas atomisation by Oerlikon GMBH (Germany). Their chemical compositions in weight percent (wt.%) determined via inductively coupled plasma (ICP) spectroscopy and combustion analysis are given in table 1. Granulometry reveals powder particle size range in between 45  $\mu\text{m}$  and 106  $\mu\text{m}$  ( $d_{50_{316L}} = 57.86 \mu\text{m}$ ;  $d_{50_{316LSi}} = 75.5 \mu\text{m}$ ).

Table 1. Chemical composition (wt.%) of 316L and 316LSi powders

	Fe	Cr	Ni	Mo	Mn	Si	N	Cu	O	P	C	S	B
316L	Bal.	17.34	12.55	2.34	1.4	0.49	0.08	0.04	0.03	0.012	<0.01	<0.01	
316LSi	Bal.	16.8	12.1	3	0.6	2.1	0.08		0.02	0.01	0.02	<0.01	0.005

## 2.2 Additive manufacturing via LDED

Thin walls with dimensions of  $100 (x) \times 12 (y) \times 0.8 (z) \text{ mm}^3$  (for tensile testing) and  $160 (x) \times 30 (y) \times 0.8 (z) \text{ mm}^3$  (for fatigue testing) were printed using a BeAM Modulo 400 LDED machine equipped with a 500W YLR-fibre laser. The printing process employed a bidirectional scanning strategy with a laser power of 250 W, scanning speed of 2000 mm/min, a powder flow rate of 6.8 g/min, a vertical displacement of focusing head of 0.2 mm after each layer deposition and a spot size of 0.7 mm. The chemical composition of the AM materials measured at FiLAB, France using ICP spectroscopy and total organic carbon analysis are given in table 2 [9].

Table 2. Chemical composition (wt.%) of AM 316L and 316LSi

	Fe	Cr	Ni	Mo	Mn	Si	N	Cu	O	P	C	S	Co	Ti	B
316L	Bal.	18.7	13.3	2.4	1.4	0.73	0.083	0.063	0.024	0.012	0.018	0.005	0.026	<0.005	0.007
316LSi	Bal.	17.4	12.2	3	0.64	2.2	0.08	0.031	0.014	0.008	0.02	0.005	0.052	<0.005	0.003

## 2.3 CW laser-SEM coupling and sample polishing

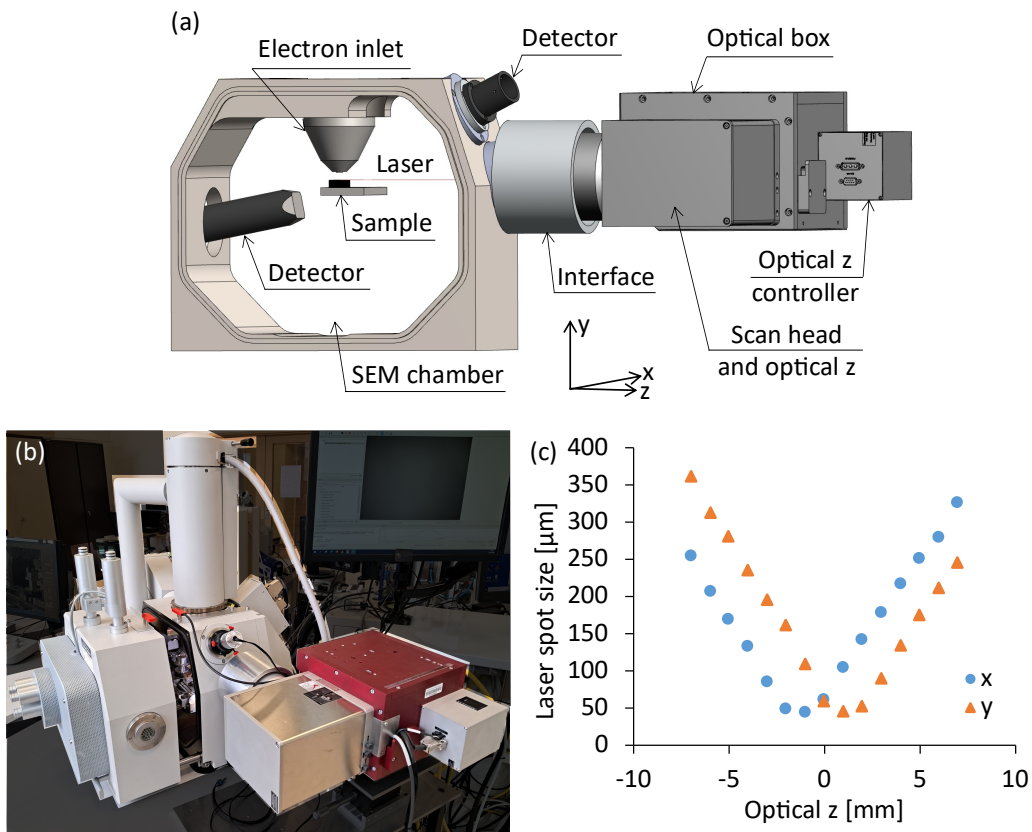


Fig. 1. CW laser-SEM coupling; illustration of the CW laser-SEM coupling (a) and image of the experimental setup (b). (c) Plot quantifying the laser spot sizes (1.7 times the full width at half maximum) in the x and y directions (in (a)) as a function of optical z (focusing distance controller)

Identifying appropriate laser scanning parameters to obtain a desired microstructure requires performing a parametric study in conjunction with microstructure characterisation before and after lasering. To facilitate such studies, a recently designed novel coupling between a CW laser and an environmental scanning electron microscope (CW laser-SEM (Fig. 1a,b)) [11] is used. While there are precedents for coupling between pulsed lasers and SEM [12–15], none exist for a CW laser-SEM. An important advantage of this coupling is its ability to perform laser scanning under secondary vacuum (pressure  $< 10^{-4}$  mbar) or under a controlled environment (e.g., inert gas environment) inside the environmental SEM. It prevents surface oxidation during lasering and facilitates a one-to-one comparison before and after scanning without additional surface preparation using different detectors available inside the SEM. The CW laser-SEM device is used to first perform a parametric study to optimise the lasering parameters. It was recently used to provide microstructural input and validate the predictions of a thermomechanical polycrystal model [16].

The CW laser-SEM is comprised of a coupling between a 1070 nm wavelength SPI QUBE 200 W air-cooled fibre laser (Industrial Laser Systems, France) and a FEI Quanta 600 environmental-SEM for characterisation (see Fig. 1a,b). The laser power can be varied from 9 to 209 W, the scanning speed from 0.01 to 20000 mm/s and the spot size from 45 to 500  $\mu\text{m}$  with the help of the incorporated Scanlab varioscan<sub>de</sub>20i type 133 (optical z). Virtually full 2D scanning liberty in a relatively large area ( $100 \times 100 \text{ mm}^2$ ) is possible with the equipped Scanlab intelliscan III 20 scanner. The laser spot sizes as a function of optical z (see Fig. 1c) and the power have been calibrated using the femto easy BP 13.9 beam profiler and gentec UP55N-40S-H9-D0 calorimeter.

Some AB 316L and 316LSi thin-walls (excluding those used for fatigue testing) were polished using 320, 600, 1200, 2400 and 4000 grit SiC paper followed by 3  $\mu\text{m}$  and 1  $\mu\text{m}$  diamond paste polishing. The final polishing step involved active oxide polishing (OPA) suspension polishing for two and a half minutes. Next, the samples (except the ones used for fatigue) were subjected to electrochemical etching using 10%vol. oxalic acid aqueous solution to reveal the microsegregations during backscatter electron (BSE) imaging. Electron backscatter diffraction (EBSD) was performed with 1  $\mu\text{m}$  step size using a Symmetry® detector (Oxford Instruments). BSE imaging is performed using an angular back scatter detector from Thermofisher.

In addition to SEM, optical microscopy (OM) is performed using the Keyence VHX-100 microscope with a VH-Z100R objective.

## 2.4 Uniaxial tensile testing

Rectangular plates with dimensions of  $35 \times 12 \times 0.8 \text{ mm}^3$  were machined from the 316L and 316LSi walls using HERMLE U 630 T, perpendicular to the DED build direction. After that, they were polished using the procedure described in section 2.3. Some of the polished plates were clamped in a small region ( $\sim 7 \times 3 \text{ mm}^2$ ) on one side and subjected to laser scanning. Dogbone specimens were extracted from AB and lasered 316L and 316LSi samples using Hermle U 630 T (see Fig. 2); sample sides were mirror polished before machining (and before lasering for lasered samples) to avoid surface roughness influence on the mechanical testing. The gauge region had the dimensions  $8 \times 4 \times 0.5 \text{ mm}^3$  ensuring a minimum length to width ratio of 2 that corresponds to the JIS Z 2241 standard; respecting this condition is sufficient for a comparative study between AB and lasered samples. Three specimens per condition were tested employing a microtesting stage at a (quasi-static) loading rate of 2  $\mu\text{m/s}$ . The use of a Sill Optics correctal camera and digital

image correlation helped to obtain the mechanical behaviour of the samples. All samples failed in the gauge region. After failure, fractography was performed on the specimens using SE imaging.

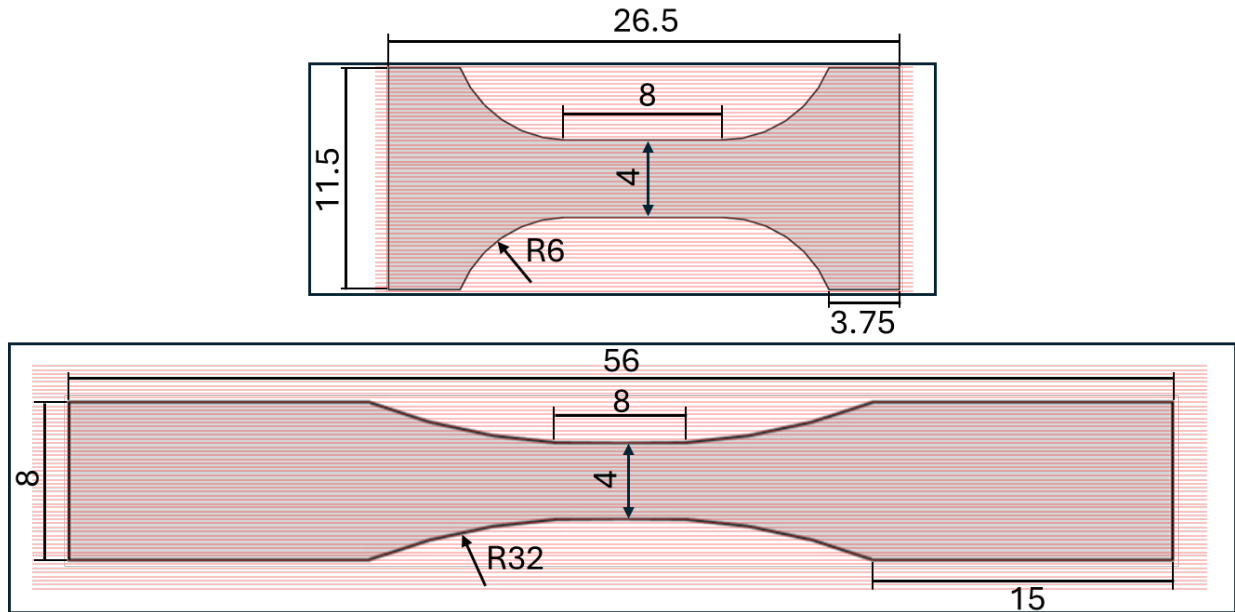


Fig. 2. Schematic of wall pieces with laser scanned region (depicted with red lines) and tensile (top) and fatigue (bottom) sample geometries

## 2.5 Scanning transmission electron microscopy and lamellae preparation

Thin-film lamellae (~100 nm thick) were extracted inside a FEI Helios Nanolab 660 dualbeam SEM microscope equipped with a focused ion beam. They were studied in the Titan<sup>3</sup> G2 TEM microscope, which is equipped with a Cs-probe corrector, scanning transmission electron microscopy (STEM) detectors and a SuperX detector. It also has the capability to perform energy dispersive X-ray spectroscopy (EDS) in order to characterise the chemical composition of the lamellae. Spectroscopy was performed with an acquisition time of 1 hour under operating conditions of 20000 counts per second and 300 keV. The spectra were deconvoluted and quantified as described in [17].

## 2.6 Residual stress measurement – X-ray diffraction

The  $\sin^2\Psi$  X-ray diffraction method was used to determine the stresses in the austenitic phase. This method is based on the measurement of Bragg peak positions for a given  $hkl$  reflection and for various directions of the scattering vector with respect to sample. Due to a significant absorption of X-rays by metals, the method only allows surface measurements. In the case of austenitic stainless steels, the average depth penetrated by X-rays at  $\Psi = 0$  is ~7.2  $\mu\text{m}$ ; the average measurement depth is defined as the depth at which 67% of the incoming intensity is reflected. Hence, the surface residual stress measures are average measures over this depth.

The residual stresses were evaluated on the surface of both sides of the specimen using the  $\Psi$  tilt method and an *in situ* diffractometer X-RAYBOT (manufactured by MRX, France). To statistically optimise the number of grains in diffraction conditions, an oscillation of  $\pm 5^\circ$  on  $\Phi$  and  $\Psi$  angles was applied during the peak's acquisitions. A collimator with a circular irradiated

area with a diameter of 2.5 mm was used. The diffraction conditions were chosen in accordance with the NF EN 15305-2009 standard: Mn- $K_{\alpha}$  radiation at 0.2290 nm wavelength, voltage 20 kV, current 1 mA, 311 ( $hkl$ ) lattice plane, diffraction angle  $2\theta = 152^{\circ}$ ,  $21 \Psi$  angles in the range  $[-37.27^{\circ}, 39.23^{\circ}]$  and  $\pm 5^{\circ}$  oscillations in  $\Phi/\Psi$ .

## 2.7 Fatigue testing

Rectangular plates with dimensions of  $70 \times 14 \times 0.8 \text{ mm}^3$  were machined from the 316L printed walls using Hermle U 630 T, perpendicular to the DED build direction (Fig. 2 bottom). After that, the plates were clamped into a customised fixture and laser scanned under secondary vacuum with scanning speed of 100 mm/s, power of 70 W, spot size of 60  $\mu\text{m}$  and scan overlap of 50%, within the CW laser-SEM chamber. As a result, a  $60 \times 12 \text{ mm}^2$  area in the centre of the plates was laser treated. Subsequently, fatigue samples with  $8 \times 4 \times 0.8 \text{ mm}^3$  gauge volume and 32 mm blending fillet (adhering to the ASTM E466-21 standard) were machined from the processed area using Hermle U 630 T. Simultaneously, the AB fatigue samples were directly machined from the unprocessed rectangular plates.

Constant amplitude uniaxial tensile fatigue test was conducted on both AB and L70 samples, using a 10 kN load cell on a Material Testing System (MTS 810), employing a sinusoidal stress waveform with a stress ratio (R) 0.1 and a constant frequency of 40 Hz, at room temperature. The loading direction was set perpendicular to the DED build direction. In order to determine the fatigue strength ( $\sigma_f$ ), the staircase method was employed. Here, the starting stresses ( $\sigma_{\text{max}}$ ) are chosen below yield strength of AB and L70 316L samples, at 275 and 325 MPa. Note that, since the difference between number of cycles corresponding to 300 MPa and 275 MPa is large, a median stress of 287.5 MPa is used for the fatigue testing. The testing was interrupted at  $3 \times 10^6$  cycles (run-outs) for samples that do not fail until that point. Fracture in all the failed samples occurred in the gauge region.

## 2.8 Surface roughness measurement

Surface roughness measurements for unpolished AB 316L and unpolished + lasered 316L samples were conducted following the ISO 25178 norm using Bruker Alicona optical system with a ring light illuminator to improve image quality. Surface texture images were captured using 20x objective lens with vertical resolution less than 13 nm, Lambda C ( $L_c$ ) filter of 80  $\mu\text{m}$ , and stitched together. MeasureSuite of Alicona was used to obtain  $S_a$ .

## 3 Results and discussion

The reference AB samples used are 316L and 316LSi stainless steel thin walls manufactured via LDED on hot-rolled 316L substrates using a single-pass-per-layer bidirectional scanning strategy with  $P$  250 W,  $v$  33.33 mm/s and  $s$  0.7 mm. These parameters result in a surface energy density  $E_s = P/(v \cdot s) = 10.71 \text{ J/mm}^2$ . EBSD imaging after mirror polishing and etching an AB sample reveals a weak texture (see Fig. S1) and a bimodal grain size distribution due to long columnar grains along layer height with a tilt along the printing direction, and smaller equiaxed grains in between layers (see upper half of Fig. 3).



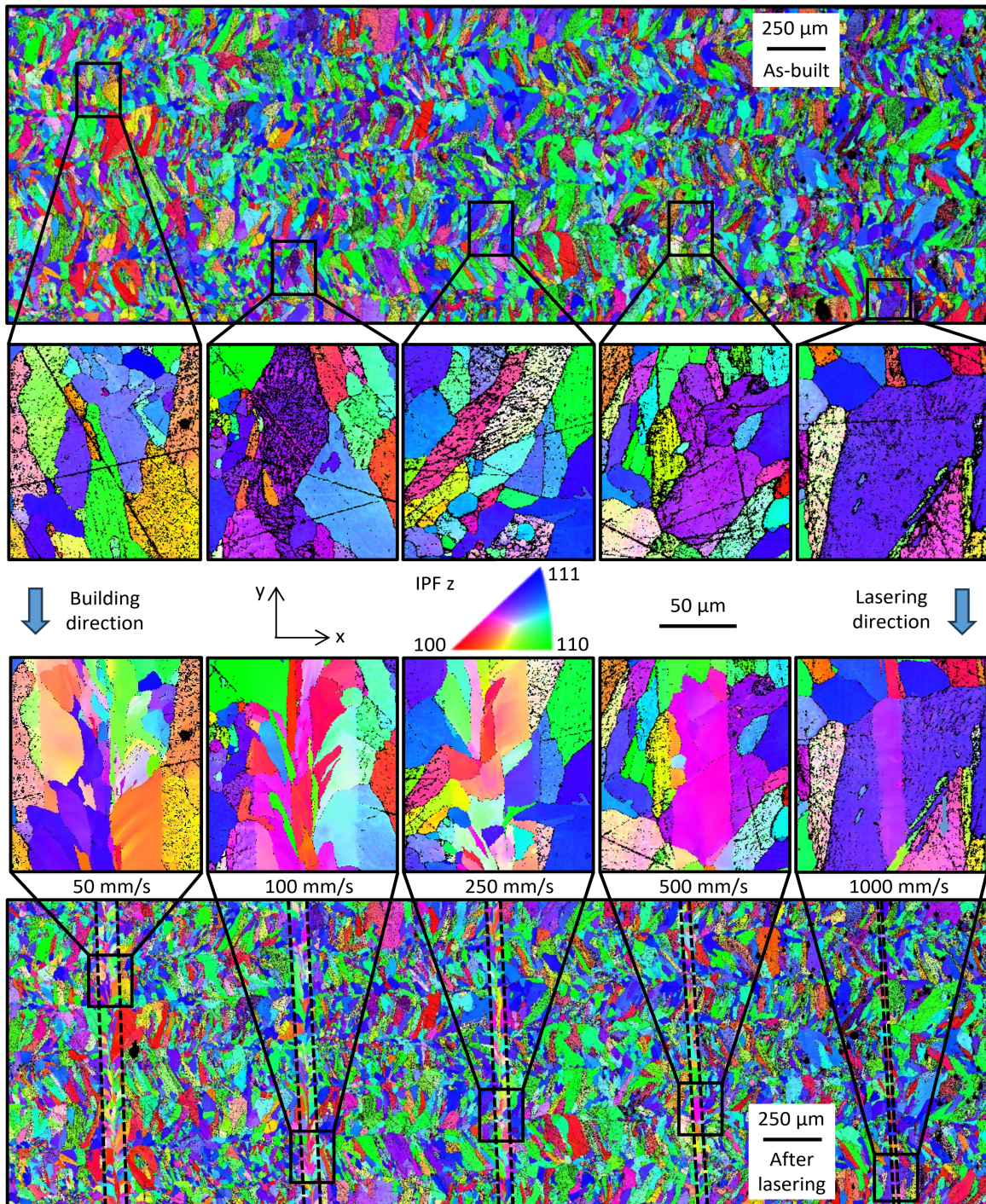


Fig. 3. EBSD IPF z images of the plane formed by building ( $-y$ ) and printing ( $x$ ) directions of the polished AB LDED 316L thin wall before and after laser scanning using  $s$  60  $\mu\text{m}$ ,  $P$  24 W and varying  $v$  (first parametric study). The scratches are consequence of polishing before laser scanning. After polishing, chemical etching is performed to facilitate BSE imaging of Cr-Mo microsegregations in Fig. 4. The noise (black dots) in the AB region of the EBSD maps is a consequence of surface undulations caused by chemical etching. Contrary to conventional practice, the scratches and the noise in all the images are deliberately left untreated in order to highlight the smoothening effect of the laser. No surface polishing was performed after laser scanning.

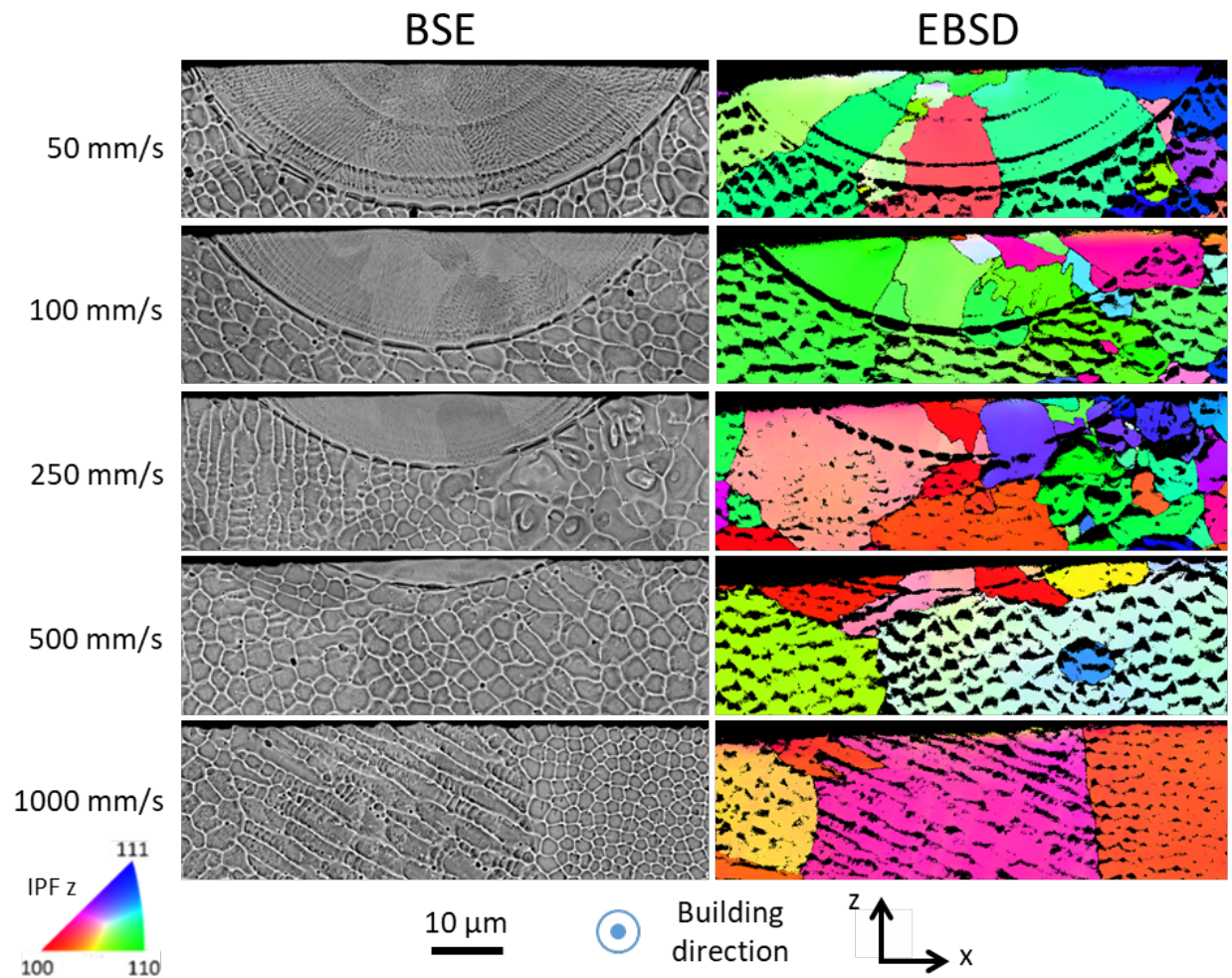


Fig. 4. BSE and EBSD IPF z images of the cross-sections across laser tracks studied in Fig. 3. The noise (black dots) in the AB region of the EBSD maps is a consequence of surface undulations caused by chemical etching to facilitate BSE imaging of Cr-Mo microsegregations. BSE and EBSD images share the same scale

The scratches in the EBSD map are a consequence of polishing defects. The noisy (non-indexed) regions are caused by chemical etching of the sample to reveal the underlying intragranular microstructure (Fig. 4). These scratches and noisy regions are deliberately kept in the images in order to highlight the surface improvement caused by laser scanning, which is discussed below.

Two parametric laser scanning studies were first conducted with 316L inside the CW laser-SEM under secondary vacuum. For both studies, a constant spot size  $s = 60 \mu\text{m}$  was used; it is an order of magnitude smaller than the one used during LDED.

### 3.1 Parametric post-process laser scanning studies: Varying scan speed, constant laser power and laser spot size

The first parametric study was performed to understand the role of varying  $E_s$  by varying  $v$  on microstructure alteration while keeping  $P$ ,  $s$  and scan strategy constant.  $P$  was set at 10% of the maximum laser power, 24 W, which is the smallest stable value for the laser used.  $s$  was set to 60  $\mu\text{m}$ , which is in the range of spot sizes used during LPBF. The scan strategy was a single line scan along the  $y$  direction (Figs. 3,4). The laser scans were parallel to each other and separated by a distance of 0.8 mm from their neighbours as seen in Fig. 3 to avoid any influence of one scan on the other. The  $v$  were chosen to correspond to five different  $E_s$  lower than the one used to manufacture the samples; since the CW laser-SEM operates under vacuum and does not use any powder feedstock, there are no convection-related heat losses or powder-related laser reflection losses; hence, a lower  $E_s$  should be needed than during the LDED process to melt the material. The five different  $E_s$  ( $v$ ) were: 8 J/mm<sup>2</sup> (50 mm/s), 4 J/mm<sup>2</sup> (100 mm/s), 1.6 J/mm<sup>2</sup> (250 mm/s), 0.8 J/mm<sup>2</sup> (500 mm/s) and 0.4 J/mm<sup>2</sup> (1000 mm/s). Laser scanning at the four highest  $E_s$  (four lowest  $v$ ) results in melting, solidification and rapid cooling of the material, whereas laser scanning at the lowest  $E_s$  (highest  $v$ ) results in heating and cooling without any apparent melting (Figs. 3,4).

The melt pool sizes of the four remelted and solidified tracks (Fig. 4) expectedly decrease with decreasing  $E_s$  (increasing  $v$ ) and their shapes reveal that conduction mode melting has occurred. The Cr and Mo microsegregation cells (a signature of rapid solidification in 316LSS [18,19]) in the lasered regions (Fig. 4) are at least an order of magnitude smaller than the ones in the AB material. Their size does not significantly decrease with increasing  $v$ , which was confirmed by comparing their sizes in the 50 mm/s and 500 mm/s tracks. The cell size difference between AB and lasered samples strongly indicates that solidification rates occurring during laser scanning are faster than those occurring during the LDED process, and they increase with increasing  $v$ . For the slowest laser scan (50 mm/s), the clearly visible microsegregation cells have an internal diameter that is  $\sim 300$  nm on average. Assuming this value to be the primary cellular arm spacing ( $\lambda$ ) during solidification, and using the empirical formula (originally designed for secondary dendritic arm spacing)  $\lambda = 80/\dot{T}^{1/3}$  for stainless steels [20], the deduced solidification rate ( $\dot{T}$ ) in the slowest laser scanned region is  $\sim 1.9 \times 10^7$  K/s; in comparison, the microsegregation cells in the AB 316L have a size of  $\sim 2.2$   $\mu\text{m}$  and the corresponding  $\dot{T}$  is slower by three orders of magnitude. At such large solidification rates, and corresponding high temperature gradients, the  $\gamma$ -austenite grains epitaxially grow from the melt pool boundary via cellular solidification mode and bend along the laser scanning direction [21], which is evidenced in the EBSD images in Figs. 3,4. In a recent work by Chen et al. [9] involving the same LDED 316L used in this work, it has been argued that either primary austenite or primary austenite with secondary ferrite mode occur during AM, which strongly supports the occurrence of cellular solidification.

Following solidification, internal and sample constraints result in the formation of thermal stresses in the heat-affected solid. These stresses are sufficiently high to cause some of the grains to undergo plastic deformation e.g., via dislocation dynamics, which can be deduced from the presence of misorientation bands observed in some grains in the remelted zone (see kernel average misorientation map in Fig. S2).

After lasering, a remarkably cleaner (higher indexation) surface is obtained along all tracks. The cleaner surfaces are primarily a consequence of remelting (under vacuum, resulting in a smoother and oxide free surface) and subsequent refinement of the intragranular microsegregation structure. A refined surface is also visible for the fastest laser scan, indicating that the surface could

have slightly remelted even though it is not discernible in the BSE and EBSD images of the cross-section (Fig. 4).

### 3.2 Parametric post-process laser scanning studies: Varying laser power, constant scan velocity and laser spot size

The next parametric study was performed to investigate laser penetration depth as a function of  $E_s$  but this time varying  $P$  and keeping  $v$  (50 mm/s),  $s$  (60  $\mu\text{m}$ ) and scan strategy (single line scan along the building direction) constant. Two different  $E_s$  were tested: 15 J/mm<sup>2</sup> (45 W – 20% of maximum  $P$ ) and 22 J/mm<sup>2</sup> (66 W – 30% of maximum  $P$ ) and compared with the laser scan already performed at 8 J/mm<sup>2</sup> (24 W – 10% of maximum  $P$ ). Based on the melt pool shapes (Fig. 5), the 8 J/mm<sup>2</sup> track resulted in conduction mode melting, whereas the 15 J/mm<sup>2</sup> and 22 J/mm<sup>2</sup> tracks resulted in keyhole mode melting. A pore can be observed close to the bottom of the melt pool in the 22 J/mm<sup>2</sup> laser track (black feature in the figure for 66 W), which is a signature of unstable keyhole mode melting. Such porosity is not visible in the 15 J/mm<sup>2</sup> track, however, the possibility of pores occurring elsewhere along the laser track cannot be eliminated.

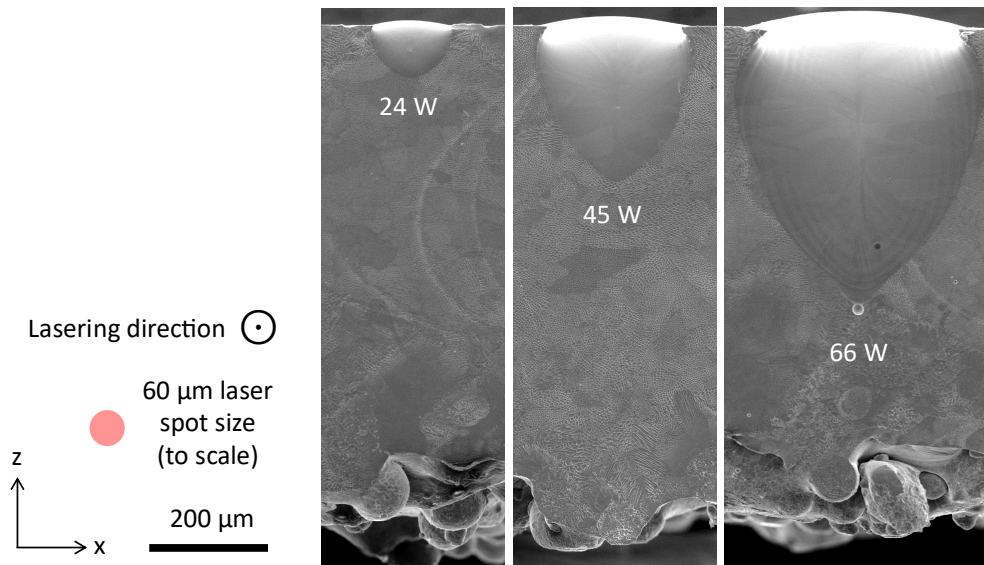


Fig. 5. BSE images showing the melt pool depths at the sample edge after laser scanning with  $s$  60  $\mu\text{m}$ ,  $v$  50 mm/s and varying  $P$  (second parametric study)

### 3.3 Summarising the parametric studies

In general, the melt pool depth increases with increasing  $E_s$ . It is more sensitive to  $P$  than to  $v$ ; e.g., the depth triples when  $P$  is increased by a factor of 1.875 from 24 W, whereas it is halved when  $v$  is increased five-fold from 50 mm/s. A transition from conduction to keyhole mode melting occurs between 8 J/mm<sup>2</sup> and 15 J/mm<sup>2</sup>. For all the scanning parameters used, cellular grain growth occurs from the melt pool boundary during solidification; this deduction is supported by the crystallographic orientations and shapes of grains (Figs. 3,4) and phase-field simulations aimed at understanding solidification during LPBF of 316L [21]. The newly formed grains have sizes similar to the unmelted ones in the base material and, as expected [21], they are bent along the

direction of laser scanning. Following solidification, tensile residual stresses are generated along the laser track during cooldown as a consequence of the temperature gradient mechanism [22]. The local stresses can be sufficiently large to trigger dislocation dynamics causing local plastic deformation, as reported in a recent *in situ* synchrotron X-ray diffraction study [23]; this argument is further supported by the misorientation bands observed in the 50 mm/s track (Fig. 3). All laser scans result in a smoother surface, which can be deduced from the disappearance of noise in the EBSD maps caused by the reduction in surface undulations induced during etching.

Based on these studies, two logical outcomes can be expected. It has already been reported that the smallest dislocation structures observed in both LDED and LPBF 316L typically either coincide with Cr-Mo microsegregation cells [3] or they are smaller than these cells [24–26]. Furthermore, smaller the size of the microsegregation cells, smaller the dislocation structures and higher the dislocation density [3,24–26]. It is well accepted that smaller (tens of nanometres) and denser feature sizes strengthen the material [27,28]. The first expected outcome is that the material in the lasered zone should exhibit smaller and denser dislocation structures, and consequently higher strength, than the AB material. Meanwhile, the observed surface refinement after laser scanning suggests that laser scanning unpolished samples should reduce the surface roughness if the laser scanning causes local melting. The second expected outcome is that the intragranular structure refinement together with a reduced surface roughness should result in an improved fatigue limit.

#### 3.4 Tensile testing polished and lasered 316L and 316LSi – improving strength-ductility tradeoff

The first expected outcome was checked by performing the following experiment. Six 35 mm-long pieces were machined from multiple AB 316L walls and polished on their largest surfaces ( $x$  and  $y$  in Fig. 3); the polishing was done to perform EBSD mapping before laser scanning and compare with the EBSD maps after laser scanning. In addition, four pieces of the same size were machined from LDED 316LSi walls. Two polished 316L and 316LSi walls were lasered on both sides (one side in its entirety before the other) using a bidirectional scan strategy with a 50% overlap (30  $\mu\text{m}$  step) between two consecutive scans and an  $E_s$  of 11.67 J/mm<sup>2</sup> using  $P$  35 W,  $s$  60  $\mu\text{m}$ ,  $v$  50 mm/s; these set of parameters, henceforth denominated L35, result in conduction mode melting, which is preferred from a manufacturing and service standpoint as it avoids creating keyhole porosities. Another two polished 316L walls were lasered on both sides with the same strategy and same  $E_s$  (11.67 J/mm<sup>2</sup>), but double  $P$  and  $v$  i.e., with  $P$  70 W,  $s$  60  $\mu\text{m}$ ,  $v$  100 mm/s (henceforth denominated L70). All laser scans were conducted under secondary vacuum. Dogbone shaped samples (Fig. 2 top) were extracted from all walls. OM, SEM, and STEM were performed before and after laser scanning. For an L70 316L sample, residual stresses were measured before and after laser scanning as well as after extracting the dogbone.

Polishing AB walls induces compressive stresses on their surfaces along both in-plane directions; e.g., a polished AB 316L wall exhibits  $\sigma_{xx} \approx \sigma_{yy} \approx -75 \pm 20$  MPa. However, subsequent laser scanning on one face followed by the other results in bending and unbending of the walls and a significant alteration of the stresses; the same sample exhibits  $\sigma_{xx} = 0 \pm 11$  MPa and  $\sigma_{yy} = 271 \pm 39$  MPa on the first lasered surface and  $\sigma_{xx} = 189 \pm 18$  MPa and  $\sigma_{yy} = 350 \pm 41$  MPa on the second lasered surface. This difference in residual stress states before and after laser scanning

implies that the sample has undergone plastic deformation during lasering. The residual stress state is further altered during dogbone extraction; the aforementioned sample exhibits  $\sigma_{xx} = -57 \pm 21$  MPa and  $\sigma_{yy} = 94 \pm 18$  MPa on the first surface and  $\sigma_{xx} = 142 \pm 15$  MPa and  $\sigma_{yy} = -34 \pm 20$  MPa on the second surface demonstrating a remarkable  $\sim 135^\circ$  rotation of the in-plane stress vector.

Continuing to focus on 316L, the melt pool shapes in the lasered zones reveal that conduction mode melting had indeed occurred (Fig. 6a). The L35 and L70 scans have respectively penetrated 8% and 14% of the total thickness of the AB walls. Both scans result in the formation of zig zag grains in accordance to the bidirectional scanning strategy used. L35 results in a weak texture, similar to the AB samples, but smaller grain sizes than the columnar grains of the AB samples (Fig. 6b). In contrast, L70 results in a strong  $\langle 100 \rangle$  texture with grains traversing multiple tracks normal to the direction of lasering. Dislocation structures and density in the lasered region are respectively smaller and higher than in the AB samples, and dislocation structures mainly coincide with the microsegregation cells (Figs. 6c,d,S3). While similar co-occurrence has been reported for LPBF 316L [3], microsegregation cells after L70 are richer in Ni-Cr-Mo-Mn-Si-O as opposed to only Cr-Mo ones reported in [3]. Furthermore, microsegregation cells in L70 samples are decorated with Mn-Si-rich oxide precipitates that are smaller in size and more evenly distributed than those occurring in LDED 316L.

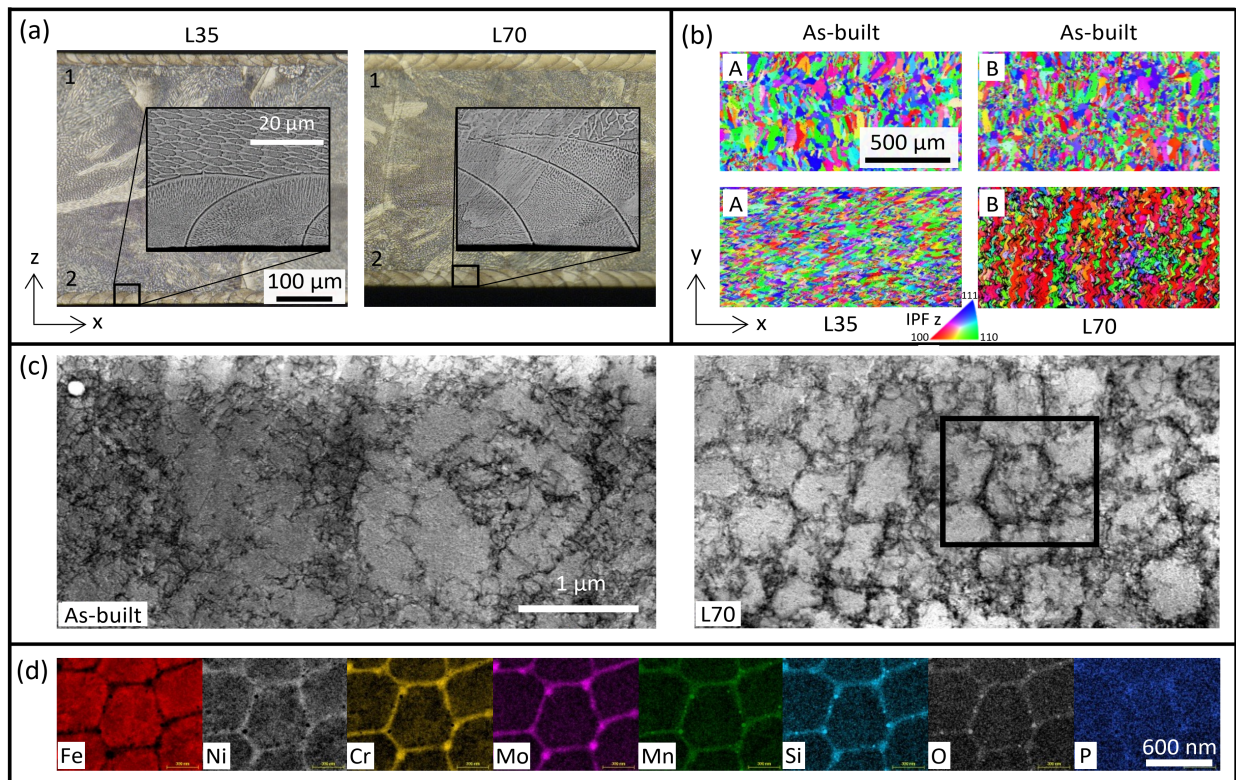


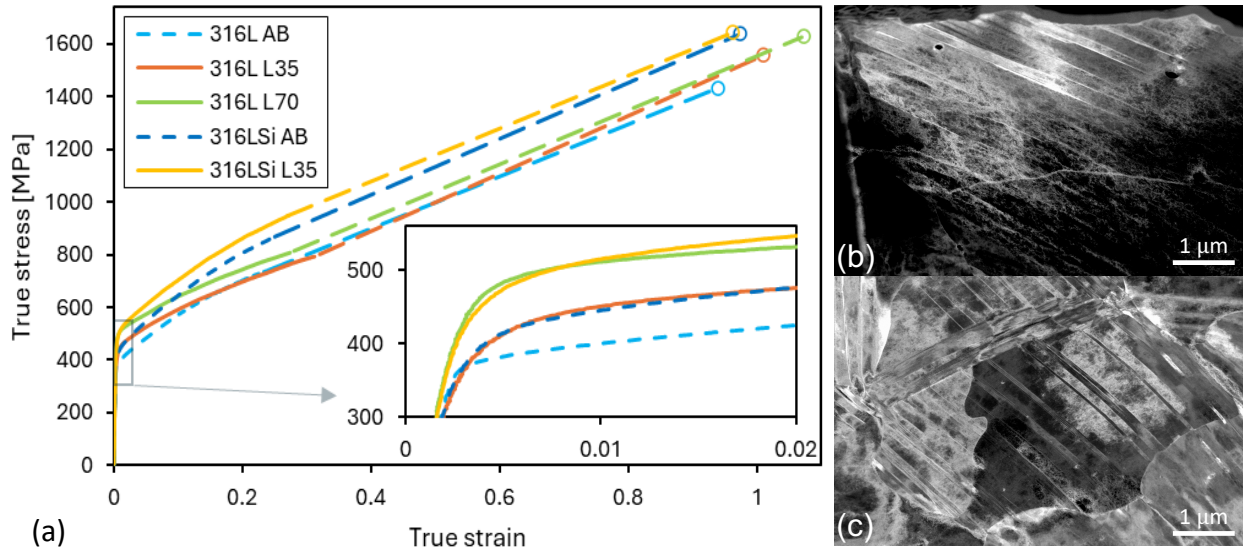
Fig. 6. (a) OM (inset BSE) images of the cross-sections of L35 and L70 316L samples. (b) EBSD images of the surface of 316L before and after L35 (A) and L70 (B). (c) Bright-field STEM images of lamellae extracted from AB and L70 316L. (d) Energy dispersive X-ray spectroscopy images from L70 revealing chemical content in the region indicated with a black box in (c)

Tensile testing reveals that AB 316L and 316LSi exhibit a mean yield strength of 360 MPa and 414 MPa, respectively (Figs. 7a,S4). Focusing on 316L, L35 and L70 result in an improvement of the mean yield strength by 11.67% and 31.11%, respectively. Using the rule of mixtures, the mean yield strengths of the lasered zones in L35 and L70 are found to be 884 MPa and 1157 MPa, respectively. To the best of our knowledge, such high yield strengths have never been reported for 316L fabricated either via LDED or LPBF. This increase in strength is primarily caused by cell refinement, changes in dislocation density, precipitate size and density and solid solution (concentration of solute atoms in the solid). Dislocation density is increased after lasering (see Fig. 6c). More precipitates are also found in the lasered material. Moreover, their size is smaller. They will have less defect probability and therefore will be less brittle, contributing more to strength and ductility. A higher solid solution is favoured in the lasered material because the cooling rate is much higher than during LDED.

The lasered region in the L70 sample exhibits a higher yield strength in comparison to existing LPBF 316L [3,5,29–34], which is a result of several factors that have a compounded effect. The key reason is the higher cooling rate that leads to smaller microstructural features, larger dislocation density and greater solid solution without the occurrence of volumetric defects such as porosity or voids. The solidification rate, calculated using the empirical formula  $\lambda = 80/\dot{T}^{1/3}$  [20], is  $\sim 1.9 \times 10^7$  K/s for the slowest laser scan (50 mm/s). This cooling rate is three orders of magnitude higher than the one for LDED, and it is also higher than the typical LPBF rate [29,30,35]. Even when the LPBF cooling rate is similar [29], judging by the cell size, there tends to be insufficient densification in LPBF, leading to poorer performance [29,31]. The cell size, which contributes very significantly to strength through a Hall-Petch like relationship [3,31], is closer to the lower end of the range for our treated material ( $\sim 300$  nm) compared to LPBF ( $\sim 200$  nm -  $\sim 2$   $\mu$ m [3,29–32,35]). The dislocation density in the cell walls appears to be higher based on the TEM data. The microstructural features also include small and dense precipitates ( $\sim 15$  -  $\sim 45$  nm; see Fig. 6d) that will further strengthen the material. Furthermore, the high cooling rate leads to higher solid solution strengthening. In addition, during the laser treatment, plastic deformation also occurs [16], which further contributes to strengthening through work hardening.

All the aforementioned factors virtuously combine in the laser treated samples to produce a strengthening effect that surpasses the typical LPBF case. A comparison with other works also demonstrates how the laser treatment improves the mechanical response in comparison to LPBF. For instance, Yin et al. [33] present a material with less coherent cell walls, lesser precipitates and longer dislocation/microsegregation cells. The shorter cells and smaller grain size for the laser treated material could also be influenced by the smaller size of the treated region, which positively contributes towards improving the strength of the material. In a similar manner, Eres-Castellanos et al. [32] present LPBF 316L with larger and longer dislocation cells and a corresponding yield strength between 760 and 985 MPa. Similarly, Dryepondt et al. [34] also present LPBF 316L with larger cells.

Meanwhile, L35 316LSi exhibits a mean yield strength of 469 MPa (an increase by 13.29%). These results together with the smaller denser dislocation structures (Fig. 6c) in the lasered zones validate the first expected outcome.



(a)

Fig. 7. (a) True stress-strain representative curves for AB, L35 and L70 316L and AB and L35 316LSi. The circles represent the stresses and strains at failure of each sample. The small dotted lines are linear connectors between the end of strain measurement and the sample failure. The inset shows a zoomed in view of the boxed region. Post-deformation dark-field STEM images of lamellae taken from (b) AB and (c) lasered zone of L70 316L samples. The 316L AB-1 and L35-1 samples have been extracted from one wall and AB-2 and L35-2 from another wall; thus, while there is a difference in strength between the two AB samples of these walls, yet L35 results in a significant increase in strength for both

All conditions fulfil the Considère criterion (Fig. 8), which means all microstructures achieve their full deformation capability prior to failure. This result is further corroborated by fractography studies (Fig. 9) showing the perfect bonding between lasered and AB regions; interestingly, the lasered region in L70 shows smaller voids, caused due to ductile damage, than in the AB region underneath as well as in the AB sample. This implies that post-process laser scanning has not adversely affected the ductility of 316L and 316LSi. In fact, L70 has resulted in a slight (9.4%) improvement in ductility of 316L (Fig. 7a). Therefore, laser scanning has resulted in a net increase in the strength-ductility tradeoff for both materials.

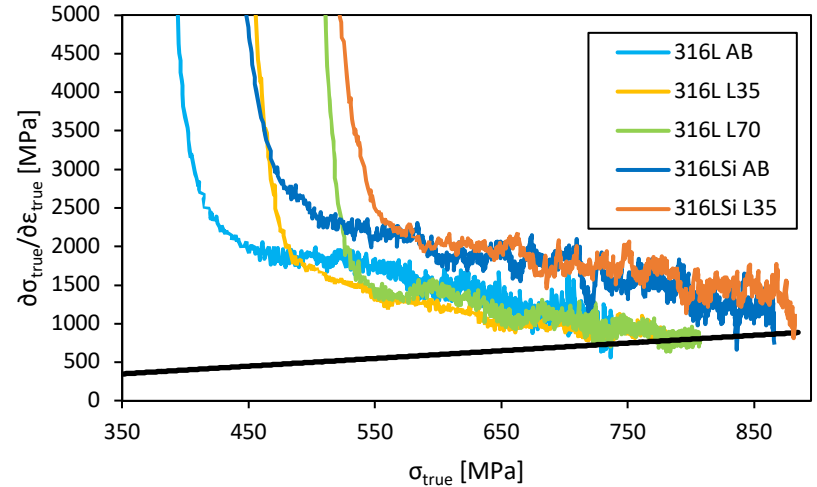




Fig. 8. Tangent modulus of the true stress-strain representative curve as a function of the true stress for AB, L35 and L70 316L and AB and L35 316LSi. The black line indicates the Considère criterion

In order to better understand the origin of no change (and even a slight improvement) in ductility, thin-film lamellae extracted post-mortem from AB and L70 316L samples were analysed via STEM. The analysis revealed that while permanent deformation in the AB 316L sample was accommodated via dislocation structure evolution, significant deformation twinning along with dislocation structure evolution had occurred in the L70 316L sample (Fig. 7b,c for AB and L70 316L, respectively); these results were confirmed with selective area diffraction maps (not shown here) and the observation of newer and smaller (than the microsegregation) dislocation cells in both AB and L70 316L samples. EDS analysis revealed that the microsegregations were not affected indicating that in the L70 sample, the finer cells do not prevent twin propagation and dislocation structure evolution. The fact that both deformation twinning and dislocation structure evolution occur in the L70 sample explain why ductility is not adversely affected after laser ing.

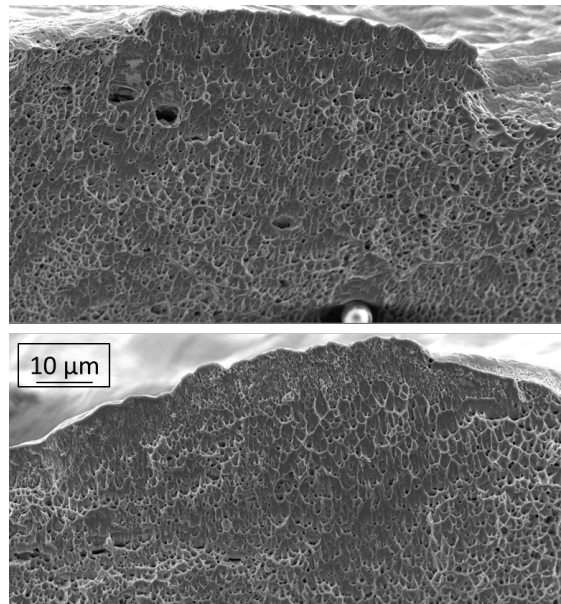


Fig. 9. Fractography of AB (Top) and L70 (bottom) 316L samples. The scale for both samples is shown in the bottom image

It should be noted that not all materials will have the possibility to accommodate deformation via multiple micromechanisms such as those occurring in 316L and therefore such an improvement in the strength-ductility tradeoff should not be *a priori* assumed for other materials.

### 3.5 Fatigue testing unpolished and lasered samples – fatigue limit enhancement

Hypothesis 2 is validated with the following experiment. Multiple 70-mm long unpolished AB 316L walls were laser scanned under secondary vacuum on both surfaces via L70. The surface roughness improved considerably with the mean surface height ( $S_a$ ) decreasing from 16.593  $\mu\text{m}$  on AB samples to 0.902  $\mu\text{m}$  after L70. Dogbone samples were extracted from unpolished AB and lasered 316L walls and subjected to tension-tension fatigue at varying stress amplitudes and mean

values. Despite the presence of tensile residual stresses due to lasering, L70 results in a significant (~25%) increase in the fatigue limit ( $\Delta\sigma$ ) from 181.94 MPa for the AB sample to 227.24 MPa (Fig. 10).

This improvement is a combined consequence of intragranular structure refinement (and the accompanying yield strength increase) along with the reduction in surface roughness. The strengthening will increase the fatigue yield threshold of the material, while the surface smoothing will remove regions of stress concentration that would allow preferential fatigue crack nucleation and growth.

It is worth commenting that the significant microstructural refinement and chemical heterogeneity reduction brought about by the treatment, together with the surface smoothing effect [7], should positively affect corrosion properties, which is a relevant aspect in processes involving the surface and sub-surface regions.

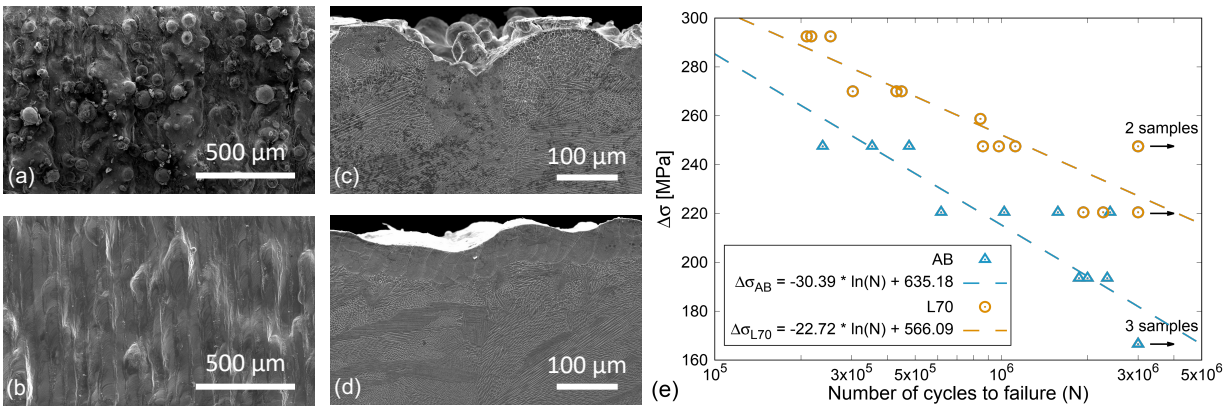


Fig. 10. Secondary electron (SE) images of the (a, b) surfaces and (c, d) cross-sections of (a, c) unpolished AB and (b, d) L70 316L walls. (e) Wöhler (S-N) curve with double the stress amplitude ( $\Delta\sigma$ ) vs number of cycles to failure (N) for tension-tension fatigue cycling of unpolished AB and lasered 316L samples. The trendlines are plotted for both samples and the arrows indicate fatigue runout cut-off at 3 million cycles

#### 4 Conclusions and perspectives

In this work, 316L and 316LSi stainless steel thin-walls fabricated via the LDED process were subjected to post-process laser scanning inside the secondary vacuum of a newly designed system coupling a continuous-wave laser and an environmental SEM, called CW laser-SEM. The two widest surfaces of the LDED thin-walls were laser scanned using parameters similar to those used in LPBF processes. The results demonstrate that lasering surfaces of as built (AB) stainless steels, using smaller spot sizes and faster scan speeds than those used during fabrication, can simultaneously significantly improve their strength-ductility trade-off and fatigue limit. Notably,

- Laser scanning resulted in the formation of sandwiched microstructures exhibiting an intragranular structure refinement in the laser melted region in comparison to the base AB material. In fact, an order of magnitude reduction in the intragranular segregation cells and dislocation cell structure was achieved in the laser scanned region, which resulted in an increase in the overall yield strength of the sample. In one case, an overall increase in the yield strength by 31.11% over the 360 MPa of the AB material was obtained after laser

scanning. For this sample, the laser penetration depth (where melting had occurred) was only 14% of the total depth of the sample. Consequently, through the rule of mixtures, a yield strength of ~1.15 GPa was obtained in the lasered region, which is significantly higher than the typical yield strengths achieved via LPBF of 316L. The microstructural and chemical heterogeneity refinement coupled with the evened surface can also be positive for the corrosion behaviour, which is particularly interesting for the studied alloys.

- This increase in yield strength occurs without any ductility loss (and even a slight improvement in one case) indicating an overall improvement in the strength-ductility tradeoff. A deeper investigation in the case of lasered 316L reveals that this improvement occurs because plastic deformation is accommodated via dislocation structure evolution as well as deformation twinning in the lasered region.
- The strength enhancement, together with the surface roughness reduction due to laser scanning, translates into a significant improvement in fatigue life. A 25% increase in fatigue limit was obtained for 316L.

Along with these results, a plethora of new interesting findings are presented, which merit deeper investigations in the future. These include (i) generation of residual stresses with strongly varying principal stresses across the sample thickness, (ii) grain structure and texture formation as a function of scan strategies keeping the energy density constant, (iii) coincidence of Ni-Mn-Si-O-rich segregations with the expected Cr-Mo segregations during solidification, (iv) reduction in the strain hardening effect after laser scanning, (v) the precise contributions of surface roughness reduction and intragranular structure refinement on fatigue limit improvement, etc.

The post-process CW laser approach has promising prospects. For example, it can be integrated within an AM process, potentially minimising or eliminating the need for extensive post-processing steps and enabling the production of net-shaped parts with superior mechanical properties. Furthermore, it creates new avenues for optimising performance of not only AM stainless steels but also other alloys, including those manufactured using other techniques.

## **Acknowledgments**

The authors acknowledge the support of the following people: Pierre-Louis Hanappier (LMS) for printing the 316L samples, Nathalie Isac (LMS) for printing the 316LSi samples, Simon Hallais (LMS) for discussions regarding SEM, Hind Meissera for assisting with the fatigue testing during their internship at LMS, and Eva Héripré (PIMM) for discussions on TEM lamellae preparation. JGSM, KC and MVU are grateful to the European Research Council (ERC) for their support through the European Union's Horizon 2020 – EXCELLENT SCIENCE – research and innovation program (grant agreement number 946959). All authors would like to thank LMS for providing financial support to build the CW laser-SEM system and IMDEA Materiales for their support in performing granulometry on the AM powder.

## **Declaration of competing interest**

The authors declare that they have no known competing financial interests or personal relationships that could have appeared to influence the work reported in this paper.

## **CRedit authorship contribution statement**

**Juan Guillermo Santos Macías:** Conceptualisation, Data Curation, Formal analysis, Investigation, Methodology, Validation, Visualisation, Writing – original draft, Writing – review & editing.

**Kewei Chen:** Formal analysis, Investigation, Validation, Visualisation, Writing – review & editing.

**Alexandre Tanguy:** Conceptualisation, Formal analysis, Investigation, Validation, Methodology, Writing – review & editing.

**Nathalie Isac:** Investigation, Visualisation, Writing – review & editing.

**Maxime Vallet:** Investigation, Visualisation, Writing – review & editing.

**Louis Cornet:** Investigation, Visualisation, Writing – review & editing.

**Vincent Michel:** Investigation, Visualisation, Writing – review & editing.

**Manas Vijay Upadhyay:** Conceptualisation, Formal analysis, Funding acquisition, Investigation, Methodology, Project administration, Resources, Supervision, Writing – original draft, Writing – review & editing, Validation, Visualisation.

**Data availability:** Data sets generated during the current study are available from the corresponding author on reasonable request.

**Code availability:** No code has been developed for this work.

## References

- [1] T. DebRoy, H.L. Wei, J.S. Zuback, T. Mukherjee, J.W. Elmer, J.O. Milewski, A.M. Beese, A. Wilson-Heid, A. De, W. Zhang, Additive manufacturing of metallic components - Process, structure and properties, *Prog. Mater. Sci.* 92 (2018) 112–224. <https://doi.org/10.1016/j.pmatsci.2017.10.001>.
- [2] T.M. Mower, M.J. Long, Mechanical behavior of additive manufactured, powder-bed laser-fused materials, *Mater. Sci. Eng. A* 651 (2016) 198–213. <https://doi.org/10.1016/j.msea.2015.10.068>.
- [3] Y.M. Wang, T. Voisin, J.T. McKeown, J. Ye, N.P. Calta, Z. Li, Z. Zeng, Y. Zhang, W. Chen, T.T. Roehling, R.T. Ott, M.K. Santala, P.J. Depond, M.J. Matthews, A.V. Hamza, T. Zhu, Additively manufactured hierarchical stainless steels with high strength and ductility, *Nat. Mater.* 17 (2018) 63–71. <https://doi.org/10.1038/nmat5021>.
- [4] J. Bedmar, A. Riquelme, P. Rodrigo, B. Torres, J. Rams, Comparison of different additive manufacturing methods for 316L stainless steel, *Mater.* 14 (2021) 6504. <https://doi.org/10.3390/ma14216504>.
- [5] Md. Shamsujjoha, S.R. Agnew, J.M. Fitz-Gerald, W.R. Moore, T.A. Newman, High strength and ductility of additively manufactured 316L stainless steel explained, *Metall. Mater. Trans. A* 49 (2018) 3011–3027. <https://doi.org/10.1007/s11661-018-4607-2>.
- [6] Y. Murakami, *Metal Fatigue: Effects of Small Defects and Nonmetallic Inclusions*, 2nd ed., Academic Press, Elsevier, Cambridge, MA, USA, 2019.
- [7] L. Chen, B. Richter, X. Zhang, X. Ren, F.E. Pfefferkorn, Modification of surface characteristics and electrochemical corrosion behavior of laser powder bed fused stainless-steel 316L after laser polishing, *Addit. Manuf.* 32 (2020) 101013. <https://doi.org/10.1016/j.addma.2019.101013>.

- [8] C. Li, D. Liu, G. Liu, S. Liu, X. Jin, Y. Bai, Surface characteristics enhancement and morphology evolution of selective-laser-melting (SLM) fabricated stainless steel 316L by laser polishing, *Opt. Laser Technol.* 162 (2023) 109246. <https://doi.org/10.1016/j.optlastec.2023.109246>.
- [9] K. Chen, J.G. Santos Macías, N. Isac, M. Vallet, L. Cornet, M. Upadhyay, Silicon mediated twin formation in laser direct energy deposited 316L stainless steel, *Scr. Mater.* (2024).
- [10] L. Hagen, Z. Yu, A. Clarke, K. Clarke, S. Tate, A. Petrella, J. Klemm-Toole, High deposition rate wire-arc directed energy deposition of 316L and 316LSi: Process exploration and modelling, *Mater. Sci. Eng. A* 880 (2023) 145044. <https://doi.org/10.1016/j.msea.2023.145044>.
- [11] A. Tanguy, M.V. Upadhyay, J.G. Santos Macías, Système pour traiter par laser à onde continue et caractériser par MEB un échantillon (Patent Pending - deposited on 16 December 2022), (Patent Pending), n.d.
- [12] K. Wetzig, J. Edelmann, W. Fischer, H. Mueller, LASEM - a novel combined device for laser modification in SEM, *Scanning* 9 (1987) 99–107. <https://doi.org/10.1002/sca.4950090303>.
- [13] A.H. Foitzik, M.W. Fütting, G. Hillrichs, L.-J. Herbst, In situ laser heating in an environmental scanning electron microscope, *Scanning* 19 (1997) 119–124. <https://doi.org/10.1002/sca.4950190211>.
- [14] M.P. Echlin, N.S. Hussein, J.A. Nees, T.M. Pollock, A new femtosecond laser-based tomography technique for multiphase materials, *Adv. Mater.* 23 (2011) 2339–2342. <https://doi.org/10.1002/adma.201003600>.
- [15] P.F. Rottmann, A.T. Polonsky, T. Francis, M.G. Emigh, M. Krispin, G. Rieger, M.P. Echlin, C.G. Levi, T.M. Pollock, TriBeam tomography and microstructure evolution in additively manufactured Alnico magnets, *Mater. Today* 49 (2021) 23–34. <https://doi.org/10.1016/j.mattod.2021.05.003>.
- [16] N. Mohanan, J.G.S. Macías, J. Bleyer, T. Helfer, M.V. Upadhyay, Intergranular stress and plastic strain formation during laser scanning of additively manufactured stainless steel: An experimentally-driven thermomechanical simulation study, *Materialia* 34 (2024) 102082. <https://doi.org/10.1016/j.mtla.2024.102082>.
- [17] M.V. Upadhyay, M.B.H. Slama, S. Gaudez, N. Mohanan, L. Yedra, S. Hallais, E. Héripéré, A. Tanguy, Non-oxide precipitates in additively manufactured austenitic stainless steel, *Sci. Rep.* 11 (2021) 10393. <https://doi.org/10.1038/s41598-021-89873-2>.
- [18] S. Kou, *Welding metallurgy*, John Wiley & Sons, New Jersey, 2003.
- [19] K.G. Prashanth, J. Eckert, Formation of metastable cellular microstructures in selective laser melted alloys, *J. Alloy. Compd.* 707 (2017) 27–34. <https://doi.org/10.1016/j.jallcom.2016.12.209>.
- [20] Th. Schubert, W. Löser, S. Schinnerling, I. Bächer, Alternative phase formation in thin strip casting of stainless steels, *Mater. Sci. Technol.* 11 (1995) 181–185. <https://doi.org/10.1179/mst.1995.11.2.181>.
- [21] A.F. Chadwick, P.W. Voorhees, The development of grain structure during additive manufacturing, *Acta Mater.* 211 (2021) 116862. <https://doi.org/10.1016/j.actamat.2021.116862>.
- [22] P. Mercelis, J. Kruth, Residual stresses in selective laser sintering and selective laser melting, *Rapid Prototyp. J.* 12 (2006) 254–265. <https://doi.org/10.1108/13552540610707013>.

- [23] S. Gaudez, K.A. Abdesselam, H. Gharbi, Z. Hegedüs, U. Lienert, W. Pantleon, M.V. Upadhyay, High-resolution reciprocal space mapping reveals dislocation structure evolution during 3D printing, *Addit. Manuf.* 71 (2023) 103602. <https://doi.org/10.1016/j.addma.2023.103602>.
- [24] T.R. Smith, J.D. Sugar, C. San Marchi, J.M. Schoenung, Strengthening mechanisms in directed energy deposited austenitic stainless steel, *Acta Mater.* 164 (2019) 728–740. <https://doi.org/10.1016/j.actamat.2018.11.021>.
- [25] A.J. Birnbaum, J.C. Steuben, E.J. Barrick, A.P. Iliopoulos, J.G. Michopoulos, Intrinsic strain aging,  $\Sigma 3$  boundaries, and origins of cellular substructure in additively manufactured 316L, *Addit. Manuf.* 29 (2019) 100784. <https://doi.org/10.1016/j.addma.2019.100784>.
- [26] K.M. Bertsch, G. Meric De Bellefon, B. Kuehl, D.J. Thoma, Origin of dislocation structures in an additively manufactured austenitic stainless steel 316L, *Acta Mater.* 199 (2020) 19–33. <https://doi.org/10.1016/j.actamat.2020.07.063>.
- [27] J. Wu, X.Q. Wang, W. Wang, M.M. Attallah, M.H. Loretto, Microstructure and strength of selectively laser melted AlSi10Mg, *Acta Mater.* 117 (2016) 311–320. <https://doi.org/10.1016/j.actamat.2016.07.012>.
- [28] J.G. Santos Macías, T. Douillard, L. Zhao, E. Maire, G. Pyka, A. Simar, Influence on microstructure, strength and ductility of build platform temperature during laser powder bed fusion of AlSi10Mg, *Acta Mater.* 201 (2020) 231–243. <https://doi.org/10.1016/j.actamat.2020.10.001>.
- [29] D. Wang, C. Song, Y. Yang, Y. Bai, Investigation of crystal growth mechanism during selective laser melting and mechanical property characterization of 316L stainless steel parts, *Mater. Des.* 100 (2016) 291–299. <https://doi.org/10.1016/j.matdes.2016.03.111>.
- [30] V.B. Vukkum, R.K. Gupta, Review on corrosion performance of laser powder-bed fusion printed 316L stainless steel: Effect of processing parameters, manufacturing defects, post-processing, feedstock, and microstructure, *Mater. Des.* 221 (2022) 110874. <https://doi.org/10.1016/j.matdes.2022.110874>.
- [31] H.E. Sabzi, E. Hernandez-Nava, X.-H. Li, H. Fu, D. San-Martín, P.E.J. Rivera-Díaz-del-Castillo, Strengthening control in laser powder bed fusion of austenitic stainless steels via grain boundary engineering, *Mater. Des.* 212 (2021) 110246. <https://doi.org/10.1016/j.matdes.2021.110246>.
- [32] A. Eres-Castellanos, A. Santana, L.M. Sanz-Moral, R. Rementeria, R.H. Pascual, M. Serrano, I. Toda-Caraballo, J.A. Jimenez, F.G. Caballero, C. Capdevila, High temperature performance of 316L steel reinforced by particle inoculation and processed by laser powder bed fusion, *J. Mater. Res. Technol.* 21 (2022) 2375–2382. <https://doi.org/10.1016/j.jmrt.2022.10.053>.
- [33] Y.J. Yin, J.Q. Sun, J. Guo, X.F. Kan, D.C. Yang, Mechanism of high yield strength and yield ratio of 316 L stainless steel by additive manufacturing, *Mater. Sci. Eng. A* 744 (2019) 773–777. <https://doi.org/10.1016/j.msea.2018.12.092>.
- [34] S. Dryepontdt, P. Nandwana, P. Fernandez-Zelaia, F. List, Microstructure and high temperature tensile properties of 316L fabricated by laser powder-bed fusion, *Addit. Manuf.* 37 (2021) 101723. <https://doi.org/10.1016/j.addma.2020.101723>.
- [35] D. Kong, C. Dong, X. Ni, L. Zhang, X. Li, Cellular size dependence on the strength of additively manufactured austenitic stainless steel, *Mater. Lett.* 279 (2020) 128524. <https://doi.org/10.1016/j.matlet.2020.128524>.